Soft Matter

The surface diffusivity of nanoparticles physically adsorbed at a solid-liquid interface

Journal:	*Soft Matter*
Manuscript ID	SM-ART-08-2024-000992.R1
Article Type:	Paper
Date Submitted by the Author:	07-Oct-2024
Complete List of Authors:	Singletary, Troy; Stony Brook University, Mechanical Engineering Iranmanesh, Nima; Stony Brook University, Mechanical Engineering Colosqui, Carlos; Stony Brook University, Mechanical Engineering

Journal Name

ARTICLE TYPE

Cite this: DOI: 00.0000/xxxxxxxxxx

The surface diffusivity of nanoparticles physically adsorbed at a solid-liquid interface

Troy Singletary,[a] Nima Iranmanesh,[a] Carlos E. Colosqui,*[a,b,c]

Received Date
Accepted Date

DOI: 00.0000/xxxxxxxxxx

This work proposes an analytical model considering the effects of hydrodynamic drag and kinetic barriers induced by liquid solvation forces to predict the translational diffusivity of a nanoparticle on an adsorbing surface. Small nanoparticles physically adsorbed to a well-wetted surface can retain significant in-plane mobility through thermally activated stick-slip motion, which can result in surface diffusivities comparable to the bulk diffusivity due to free-space Brownian motion. Theoretical analysis and molecular dynamics simulations in this work show that the surface diffusivity is enhanced when (i) the Hamaker constant is smaller than a critical value prescribed by the interfacial surface energy and particle dimensions, and (ii) the nanoparticle is adsorbed at specific metastable separations of molecular dimensions away from the wall. Understanding and controlling this phenomenon can have significant implications for technical applications involving mass, charge, or energy transport by nanomaterials dispersed in liquids under micro/nanoscale confinement, such as membrane-based separation and ultrafiltration, surface electrochemistry and catalysis, and interfacial self-assembly.

1 Introduction

The ability of physically adsorbed nanomaterials (e.g., nanoparticles, macromolecules, polyatomic ions) to move along an adsorbing surface has critical implications in numerous natural and industrial processes for water treatment, energy storage, advanced manufacturing, and other emerging technologies involving active and passive transport of nanomaterials dispersed in a liquid under confinement. For example, membrane-based separation processes are critically affected by the ability of the rejected material, the retentate, to be mobilized while adsorbed to the surface for preventing fouling and reduction of the permeate.[1–3] The surface mobility of electroactive nanomaterials can control the maximum charge transferred at an electrode in liquid electrolyte solutions or limit the access to catalytic sites and the effective reaction rate.[4–7] Similarly, the in-plane mobility of ionic species adsorbed within the so-called Stern layer leads to significant contributions to the electrical conductivity of micro/nanopores and fluidic devices employing electrokinetic flows for charge separation and energy conversion.[8–10] Understanding and predicting the surface diffusivity of nanoparticles is also relevant to advanced manufacturing technologies involving 2D self-assembly and sintering.[11–17]

The physical adsorption onto a surface of a rigid nanoparticle dispersed in a liquid solvent occurs when there is a global (stable) or local (metastable) minimum in the energy landscape resulting from all molecular interactions between the particle, surface, and solvent.[18–20] The adhesion process is considered as irreversible when the energy increase to escape the stable (or metastable) minimum is much larger than the thermal energy of the system k_BT (here, k_B is the Boltzmann constant, T is the system temperature).[21–23] Furthermore, the adsorbed particle is "immobilized" in a given direction when the width of a large energy well in such direction is much smaller than the particle dimensions.[24–26] These basic considerations, however, are dependent on the observation time scales and the dimensionality of the energy landscape, which can make highly nontrivial the rationalization of the post-adsorption behavior of a nanoparticle.

The 1D potential of mean force (PMF) $U(d)$ as a function of the particle-surface separation distance d is commonly predicted by the Derjaguin-Landau-Verwey-Overbeek (DLVO) theory,[19,27,28] considering van der Waals (vdW) and electric double layer (EDL) forces, and predicts a single (stable) energy minimum at direct particle-wall contact for which finite contact separation $d_0 \simeq \sigma/2$ is prescribed by the characteristic molecular diameter σ. However, energy minima at multiple nanoscale separations $d - d_0 > 0$ can be produced by solvent-induced interactions (e.g., the oscillatory structural force) due to the molecular reconfiguration of the solvation or hydration layers confined between the particle and the wall.[29–34] Previous work has documented that such solvent-induced interactions not considered by DLVO theory

[a] Mechanical Engineering Department, Stony Brook University, Stony Brook, NY 11794, USA
[b] Applied Mathematics & Statistics Department, Stony Brook University, Stony Brook, NY 11794, USA
[c] The Institute of Energy: Sustainability, Environment, and Equity, Stony Brook University, NY 11794
* E-mail: carlos.colosqui@stonybrook.edu

can lead to the kinetic trapping of rigid nanoparticles at periodic separations $s \simeq n\sigma$ ($n > 0$ is an integer number) for which the particle is effectively immobilized in the direction normal to the adsorbing surface while retaining substantial in-plane translational mobility.[35–38]

This work proposes an analytical model to predict the (in-plane) surface diffusivity $D_{\parallel}$ of physically adsorbed nanoparticles of rigid materials by considering hydrodynamic friction effects along with spatial fluctuations of the PMF due to nanoscale solvent-induced interactions in the solvation layers confined between the particle and adsorbing surface. These solvation-induced interactions lead to both the kinetic trapping of the nanoparticle at finite separations from the solid wall and "stick-slip" motion parallel to the surface. The proposed model requires as input parameters basic material properties that are experimentally determinable (i.e., zero-shear bulk viscosity, interfacial surface energies, Hamaker constants) and therefore is applicable to general solid materials and liquid solvents. Theoretical predictions are verified by molecular dynamics (MD) simulations for the case of small rigid nanoparticles with a range of typical Hamaker constants and interfacial surface energies that correspond to common metal oxides and polymeric materials, which are moderately wettable by water and simple molecular solvents.

2 Theoretical Analysis

2.1 Potential of Mean Force Model: Near-Contact Conditions

Adopting a continuum (mean-field) description, we will formulate a simple two-dimensional expression for the effective PMF $U(d,s)$ of a quasi-spherical rigid nanoparticle of radius R that is fully immersed near a planar wall, in terms of the nanoscale separation distance d and in-plane displacement s (cf. Fig. 1a). We consider that solvent-induced interactions arise at small nanoscale separations due to the formation and re-arrangement of a 3D pseudo-crystalline liquid structure in the solvation layers near a wettable surface. This leads to separation-dependent oscillatory structural forces with a characteristic energy U_s, that decay exponentially away from the wall with a period prescribed by the liquid molecule diameter σ.[19,32,33] In-plane displacements produce a periodic shear deformation and dislocation of the 3D solvation structure that result in energy oscillations with amplitude $U_{\parallel}$ and a period prescribed by the characteristic interactomic separation $\Delta x \sim \sigma$ between solid atoms on the solid surface.

The PMF for the nanoparticle is therefore formulated as

$$U(d,s) = U_{DLVO} + U_s e^{-\frac{d}{\sigma}} \cos\left(\frac{2\pi d}{\sigma}\right) \times \left(1 - \frac{\beta}{2}\cos\left(\frac{2\pi s}{\Delta x}\right)\right) \quad (1)$$

where U_{DLVO} is the energy from classical (particle-wall) DLVO interactions, U_s is the characteristic adhesion or de-wetting energy due to the modeled solvent induced interactions, and β is given by the ratio between the characteristic in-plane energy oscillation and adhesion energy. The characteristic energy of adhesion due to solvent-induced interactions is[38]

$$U_s = -2\bar{\gamma}\pi R_c^2, \quad (2)$$

where $\bar{\gamma} = (\gamma_1 + \gamma_2)/2$ is the average interfacial energy determined by the interfacial surface energies (energy per unit area) γ_i $(i = 1,2)$ for the particle and the wall surface, and $R_c = R\sqrt{1-(1-\sigma/R)^2}$ is the effective contact radius determined from the area $S_c \simeq \pi R_c$ removed from the first solvation layer when direct particle-wall contact is attained (cf. Fig. 1b).

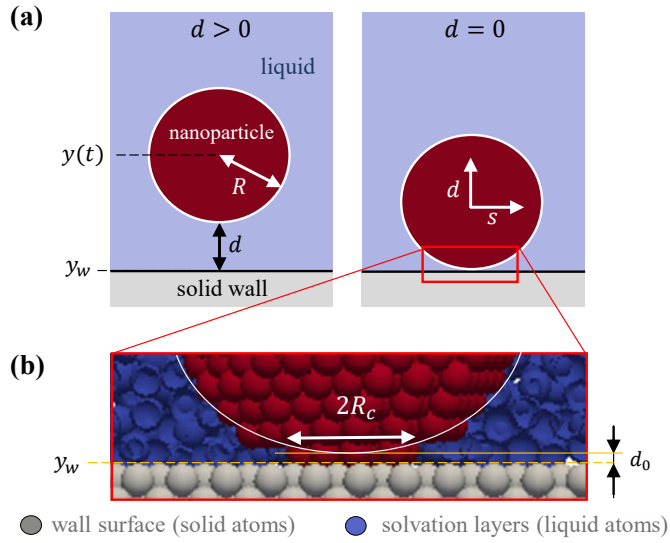

Fig. 1 Nanoparticle near an adsorbing surface in liquid media. (a) Continuum description: a spherical rigid nanoparticle of radius R lies near a planar wall at a separation distance d. Particle-wall contact occurs at a single point for which $d = 0$. The particle PMF $U(d,s)$ is parameterized by the particle-wall separation distance d and the in-plane displacement s. (b) Atomistic description: a quasi-spherical nanoparticle formed by atoms or molecules of finite diameter σ makes contact with the wall over a finite surface area $S_c = \pi R_c^2$ at an average separation $d_0 \simeq \sigma/2$. The contact radius $R_c = R\sqrt{1-(1-\sigma/R)^2}$ is then determined from the surface area S_c removed from the first solvation layer to attain contact.

The PMF in Eq. 1 introduces a periodic energy barrier $\Delta U_{\parallel}$ for in-plane motion through similar simplifications as the classical Frenkel-Kontorova model for contact friction and stick-slip motion on the atomic scale.[39–41] We consider that the energy per unit area required to shear/dislocate the wetting liquid structure, by breaking and forming the solvation layers to regenerate wetted surface area as the particle moves parallel to the wall, is comparable to the particle-liquid interfacial energy $\gamma_{pl} \sim k_B T/\sigma^2$ to create solid-liquid interface (see Sec. 3.1). Hence, the in-plane energy barrier for a physically adsorbed nanoparticle is expressed as

$$\Delta U_{\parallel}(d) = 2\beta \frac{k_B T}{\sigma^2} \pi R_c e^{-\frac{d}{\sigma}} \cos\left(\frac{2\pi d}{\sigma}\right) \quad (3)$$

for $|d - d_n| \leq \sigma/2$, where the metastable separation distances $d_n = d_0 \simeq n\sigma$ are prescribed by an integer number n of molecular layers, and the factor β, taking values $0 \leq \beta \leq 1$, accounts for static and dynamic effects reducing the effective energy barrier for in-plane displacements. Such effects include "defects" in the sheared quasi-crystalline solvation structure, particle rotation and misalignment with the wall plane, and correlated displacements of the particle and wetting liquid molecules.[42–44]

DLVO interactions near contact. The PMF formulated in Eq. 1 is valid for near-contact conditions, under which the oscilla-

tory structural force is the dominant contribution from solvent-induced interactions and vdW forces are the dominant DLVO interaction. For this analysis we will thus adopt

$$U_{DLVO} = -\frac{AR}{6(d+\frac{\sigma}{2})} \quad (4)$$

where A is the Hamaker contact for particle-wall interactions in the liquid medium. The vdW interactions dominate over electrostatic effects for weak surface charge $\sigma_s \ll 1.84\sqrt{A\varepsilon/(24\pi\lambda_D^3)}$ and small separations $d < R$, or moderate-to-large surface charge and nanoscale separations $d \sim \sigma \lesssim \sqrt{A\varepsilon/(24\pi\sigma_s^2\lambda_D)}$; here, ε is the solvent dielectric and λ_D is the Debye length prescribed by the ion concentration n_0. For charge regulating surfaces and electroneutral systems one has $|\sigma_s| \lesssim \sqrt{8n_0\varepsilon k_BT}$ [45,46] and the near-contact conditions modeled by Eq. 1 would correspond to $d \lesssim$ 1-3 nm (i.e., 3 to 10 molecular diameters) in the case of moderate Hamaker constants ($|A| =$ 5-10 k_BT) and ion concentrations (0.01 and 1 mM) of a symmetric 1:1 electrolyte in aqueous solution.

Metastable adhesion and off-plane kinetic trapping. The solvent-induced interactions modeled in Eq. 1 produce local energy minima at a finite number of nearly periodic distances $d_n \simeq d_0 + n\sigma$ $(n = 1, \infty)$ that satisfy the condition [38]

$$e^{-\frac{d_n}{\sigma}}\left(\frac{d_n}{\sigma}+\frac{1}{2}\right)^2 \geq \frac{|A|}{|\bar{\gamma}|\sigma^2} \times \left(\frac{R\sigma}{24\pi^2 R_c^2}\right), \quad (5)$$

where we use $\sqrt{1+4\pi^2} \simeq 2\pi$. According to Eq. 5, metastable adhesion at finite separations of 1 to 4 molecular layers is expected for small nanoparticles of radius $R \lesssim 100$ nm and conventional rigid materials for which $|A| \lesssim 20k_BT$ and $|\bar{\gamma}| \lesssim 3k_BT/\sigma^2$, in aqueous solutions for which $\sigma \simeq 0.3$ nm. The PMF in Eq. 1 additionally predicts that particle-wall contact can be effectively prevented due to a kinetic trapping phenomenon when $|U(d_n - \sigma/2, 0) - U(d_n + \sigma/2, 0)| > k_BT$. [38] Fully preventing the kinetic trapping and achieving particle-wall contact with stable adhesion at $d = d_0$ requires Hamaker constants larger than a critical value [38]

$$A_c = \left(0.465\pi R_c^2|\bar{\gamma}| - k_BT\right) \times (22.5\sigma/R). \quad (6)$$

Eq. 6 predicts that quasi-spherical nanoparticles with $R \gg \sigma$ can attain contact for Hamaker constants larger than $A_c = 65.7|\bar{\gamma}|\sigma^2$, which corresponds to moderately large Hamaker constants $A \gtrsim$ 20-60 k_BT for the case of common hydrophilic materials (e.g., metal oxides) in aqueous media.

2.2 Surface Diffusivity

To rationalize the surface diffusivity of a physically adsorbed sub-100-nm nanoparticle we will consider that the particle can be "trapped" at metastable separations $d_n \simeq d_0 + n\sigma$ within a few molecular layers ($n = 1, 4$), according to Eq 5, and that direct "dry" contact is prevented over long times when the Hamaker constant is smaller than the critical value predicted by Eq. 6. [38] According to the PMF model in Eq. 1 thermally activated stick-slip motion parallel to the surface arises while the particle is adsorbed at metastable separations d_n; i.e., the particle "sticks" when trapped at local minima for which $\partial U/\partial s = 0$ and "slips" when rapidly crossing over an energy barrier of magnitude $\Delta U_\parallel$ in the in-plane direction. Hence, a substantial effective diffusivity is expected for negative (repulsive) or weakly positive (attractive) Hamaker constants smaller than the critical value A_c predicted by Eq. 6.

The effective diffusivity, determined from the mean square displacement (MSD) in a specific direction of motion, is prescribed by (1) dissipative effects (e.g., hydrodynamic drag) determined by a friction coefficient ξ and (2) kinetic effects controlled by the magnitude of energy barriers ΔU along such direction of motion. [24,47–50] Such dissipative and kinetic effects can be highly local and anisotropic in the presence of liquid-solid interfaces. [42–44,51] The in-plane diffusivity $D_\parallel$, as well as the off-plane diffusivity $D_\perp$, near contact is generally expected to differ significantly from the diffusion constant $D_0 = k_BT/\xi_0$ in the isotropic liquid bulk, which is prescribed by the free-space drag coefficient ξ_0 in the absence of energy barriers hindering thermal motion. [52–55] The in-plane hydrodynamic friction coefficient can be conveniently expressed as $\xi_\parallel = \lambda_\parallel(d)\xi_0$ where $\lambda_\parallel(d)$ is a separation-dependent correction factor and $\xi_0 = 6\pi\mu R'$ is the free-space Stokes drag determined by the shear viscosity of the liquid and the hydrodynamic or solvated radius R' of the nanoparticle. [56,57] The thermally activated crossing of in-plane energy barriers is a random process with a kinetic rate $\Gamma_\parallel = \Gamma_0 \exp(-\Delta U_\parallel/k_BT)$ where the attempt rate $\Gamma_0 = 2D_\parallel/\sigma^2$ is estimated from the time to diffuse between neighboring minima under pure Brownian motion. [24,47–50] From the in-plane mean square displacement $MSD_\parallel(1/\Gamma_\parallel) = \sigma^2 = 2D_\parallel/\Gamma_\parallel$ due to thermally activated crossings between neighboring minima one can estimate the effective surface diffusivity $D_\parallel(d) = D_0 \exp(-\Delta U_\parallel/k_BT)$.

Considering dissipative and kinetic effects near contact conditions the nanoparticle surface diffusivity is thus given by

$$D_\parallel(d) = D_0 \times \lambda_\parallel \times e^{-\Delta U_\parallel/k_BT}, \quad (7)$$

where $\Delta U_\parallel$ is defined in Eq. 3 and the hydrodynamic friction factor is analytically estimated as

$$\lambda_\parallel(d) = 1 + \frac{1}{6}\frac{R'^2_c}{R'd}, \quad (8)$$

by adding to the Stokes drag for a sphere the shear drag of a planar circular facet with a solvated radius R'_c moving parallel to the wall at a small separation distance $d < R$; we will employ in this expression the hydrodynamic or solvated radii $R' = R + 2\sigma$ and $R'_c = R_c + 2\sigma$ based on MD simulation results for the studied conditions (see Sec. 3). Predictions from Eqs. 7-8 with the PMF modeled in Eq. 1 will be compared with MD simulations described in the following section for a range of conditions commonly encountered for rigid nanoparticles of conventional metal oxides [58–60] (e.g., Fe_3O_4, SiO_2, TiO_2) or polymeric materials. [61–63]

3 Molecular Dynamics

To verify the analytical model for the surface diffusivity proposed in Sec. 2 we perform MD simulations with the open-source package LAMMPS [64] for single quasi-spherical rigid nanoparticles subject to thermal motion while physically adsorbed onto a plane wall fully immersed in liquid. The MD simulations in this

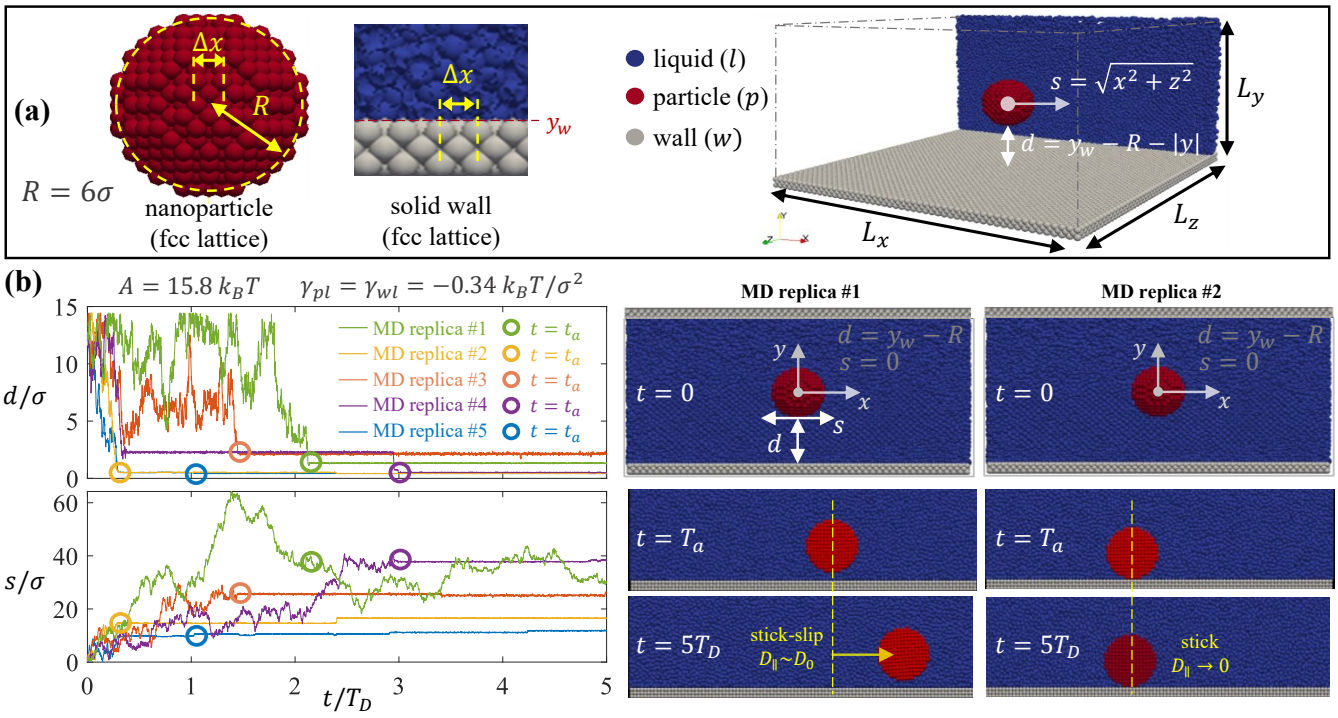

Fig. 2 Molecular dynamics simulations of nanoparticle adsorption and surface diffusion. (a) Atomistic representation of the modeled quasi-spherical rigid nanoparticle ($R = 6\sigma$) and planar wall. The periodic simulation domain has the top/bottom walls located at $y = \pm y_w = \pm 20\sigma$ and is filled with the modeled liquid. The particle-wall distance $d(t) = y_w - R - |y|$ and in-plane displacement $s(t) = \sqrt{x^2 + z^2}$ are computed from the center-of-mass position $\mathbf{x}(\mathbf{t})$ reported by the MD replica simulations. (b) Replica MD simulations (five) for each of the studied eleven conditions (see Table. 1) report different separation distances $d(t)$ and in-plane displacements $s(t)$ (color lines). Metastable adhesion or contact occurs at a random time T_a (see circles) after which the separation distance $d(t > T_a) \simeq \bar{d}$ remains nearly constant. The particle can perform stick-slip motion or remain immobile after adhesion (cf. right panels). The reported MD replicas correspond to $A = 15.8 k_B T$ and $\gamma_{pl} = \gamma_{wl} = -0.34 k_B T/\sigma^2$.

work are not intended to model any specific solid or liquid (e.g., polar/non-polar solvents) but to produce the DLVO and solvent-induced interactions considered in the analytical expressions in Sec. 2 through measurable material properties. Three different atomic species model the liquid solvent (l), solid particle (p), and wall (w), the three atomic species are modeled with the same van der Waals diameter σ, atomic mass m, and zero charge. The particle and wall number densities $n_p = n_w = 1/\sigma^3$ are uniform and equal, and the bulk number density of the liquid is $n_l = 0.8/\sigma^3$. The simulation domain is a 3D periodic box ($L_x = 80\sigma$, $L_y = 42.5\sigma$, $L_z = 80\sigma$) fully filled with the modeled liquid solvent and confined along the y-direction by a plane wall located at $y = \pm y_w$; here, the wall coordinate $y_w = 20\sigma$ is defined by the plane where liquid and solid molecules of finite size σ get in contact (see Fig. 2a). A quasi-spherical nanoparticle of radius $R = 6\sigma$ (i.e., ~ 4 nm diameter) is carved out of a fcc lattice with uniform spacing $\Delta x = 4^{1/3}\sigma$ and the plane wall is a "frozen" fcc lattice with the same uniform spacing Δx (cf. Fig. 2a). All the MD simulations are performed in the NVT ensemble with a Nose-Hoover thermostat to maintain constant system temperature for the particle and liquid.[65]

The MD simulations in this work employ the standard 12-6 Lennard-Jones (LJ) pairwise potential $U(r) = 4e_{ij}[(\sigma/r)^{12} - (\sigma/r)^6]$, where e_{ij} is the characteristic interaction energy between different species ($i, j = l, p, w$) and r is the distance between any two atoms. The LJ potential is used with a cutoff distance $r_c = 2.5\sigma$ for liquid-liquid and solid-liquid interactions and $r_c = 4\sigma$ for particle-wall interactions, which improves computational efficiency while accurately representing interatomic forces.[66,67] The standard LJ potential models pairwise hard-core repulsion and non-retarded vdW attraction between different atomic species, which collectively gives rise to the DLVO and solvent induced-interactions[38,51,68–70] considered in the PMF model in Eq. 1.

Replica simulations. Five MD replica simulations per case are performed by initializing the atomic velocities with different random values producing the same system temperature T and letting the system energy equilibrate with the particle fixed at the center of the domain (cf. Fig. 2b). After the equilibration step the nanoparticle is free to translate and rotate as a rigid body, the equations of motion for the particle and liquid atoms are integrated with a small timestep $\Delta t = 0.01\sqrt{k_B T/m\sigma}$. Under the modeled conditions the liquid has a constant bulk shear viscosity $\mu = 2.1\sqrt{mk_B T}/\sigma^2$.[71,72] The Stokes-Einstein relation $D_0 = k_B T/(6\pi\mu R')$ with a hydrodynamic radius $R' = R + 2\sigma$ accounts for the particle diffusivity determined from free-space MD simulations within a 15% relative error for all the studied cases.[38] As reported in Table 1 these replica simulations are performed for eleven different conditions by using a set of different interaction energies for the particle-liquid LJ energy $e_{pl} = 0.5$-$1.5\ k_B T$ and wall-liquid energy $e_{wl} = 0.5$-$1.5\ k_B T$, while the LJ energy is $e_{ii} = k_B T$ for all self-interactions and $e_{pw} = k_B T$ for the pairwise particle-wall interactions. This set of pairwise

interaction energies produces five different Hamaker constants $A = 4\pi^2\sigma^6 n_p(n_w e_{pw} - n_l e_{pl})$ = -7.9, 0, 7.9, 15.8, & 23.7 k_BT, and five different interfacial energies $\bar{\gamma} = (\gamma_{pl} + \gamma_{wl})/2$ = -0.23, -0.34, -0.6, -0.81, & -1 k_BT/σ^2, as described in Sec. 3.1.

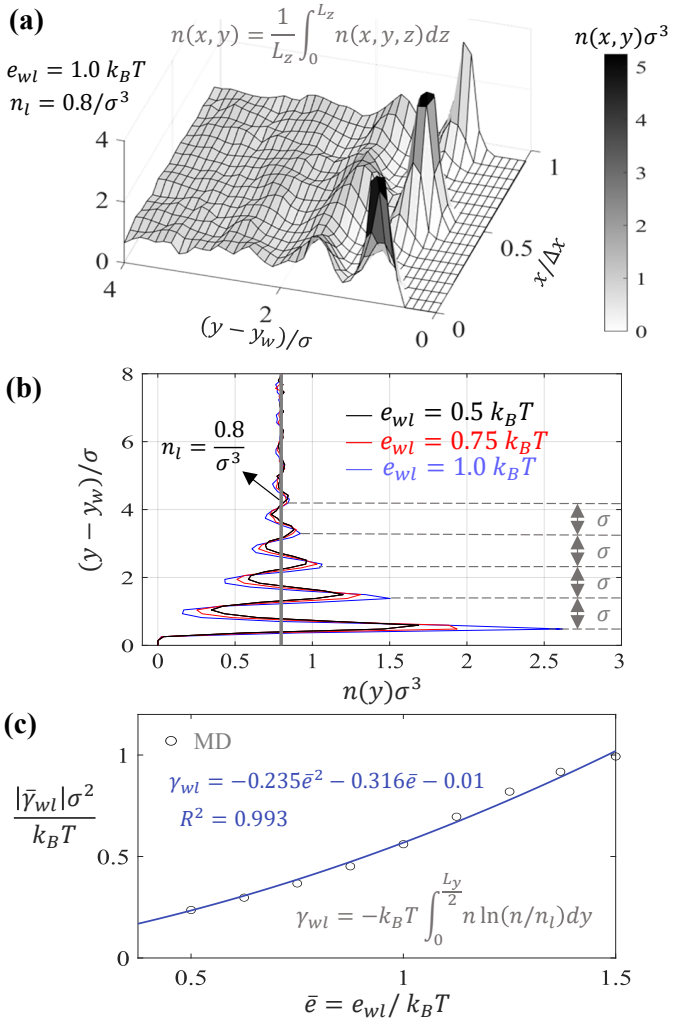

Fig. 3 Liquid structure and solvation layers near a planar wall. (a) The 2D liquid density field $n(x,y) = n(z,y)$ computed from MD presents periodic spatial variations of comparable magnitude in the direction normal and parallel to the wall, indicating the presence of off- and in-plane energy barriers induced by the liquid solvation structure. (b) The 1D liquid density profile $n(y) = (1/L_x)\int_0^{L_x} n(x,y)dy$ shows local energy minima in the liquid solvation structure with a period similar to the liquid molecule diameter σ. The density profiles, reported for three different solid-liquid interaction energies e_{wl} = 0.5, 0.75, & 1 k_BT, show that density fluctuations decay nearly exponentially away from the wall and their magnitude increases monotonically with the pairwise LJ energy e_{wl}. (c) Solid-liquid interfacial energies γ_{wl} computed from MD via the 1D density profile $n(y)$. For the modeled conditions, $|\gamma_{wl}|$ increases with the pairwise energy e_{wl} following a nearly quadratic relation (see fit to the MD data).

The MD simulations report the instantaneous center-of-mass position of the nanoparticle, $\mathbf{x}(t) = x\mathbf{i} + y\mathbf{j} + z\mathbf{k}$, from which the wall-particle separation distance $d = y_w - R - |y(t)|$ and in-plane displacement $s(t) = \sqrt{x^2 + z^2}$ are readily determined. All the replica simulations are initialized with the nanoparticle at the center of the simulation domain at an initial separation $d(0) = y_w - R$ from the top/bottom walls and run over the same simulation time $T_s \simeq 5d(0)^2/D_0$ that is nearly five times the diffusive time $T_D = d(0)^2/D_0$ to reach the (top or bottom) wall under free-space Brownian motion. Metastable adhesion or contact in each replica simulation occurs at a random adhesion time T_a, after which the nanoparticle remains "trapped" near a finite distance $d_n - d_0 \simeq n\sigma$ $(n = 0,4)$ undergoing extremely small off-plane displacements $|d(t > T_a) - d_n| \ll \sigma$ that result in a vanishing off-plane diffusivity $D_\perp \to 0$ for $t > T_a$ (cf. Fig. 2b). Notably, the nanoparticle can retain substantial in-plane diffusivity $D_\parallel(d) \lesssim D_0$ through stick-slip motion after metastable adhesion at finite separations $\bar{d} - d_0$ = 1-4 σ of one to four molecular layers from the wall for certain studied combinations of sufficiently low Hamaker constant and large magnitude of the interfacial surface energy (cf. Table. 1).

3.1 Solvation structure and interfacial energy

The solid-liquid interfacial energy and local free energy of the liquid can be effectively determined from the equilibrium number density via conventional mean-field approximations.[34,38,73] To determine the number density field from MD we perform a set of supplementary simulations with the modeled liquid confined by the plane wall as reported in Fig. 2a but without a nanoparticle. As shown in Fig. 3a, the 2D number density field $n(x,y) = n(z,y) = (1/L_z)\int_0^{L_z} n(x,y,z)dz$ computed from the time-averaged 3D positions of liquid atoms presents off-plane and in-plane spatial fluctuations near the wall with similar magnitude a period comparable to the atomic diameter σ. This phenomenon corresponds to the formation of a 3D quasi-crystalline structure in the solvation layers near the wall and gives rise to the solvent-induced interactions approximately modeled in Eqs. 1–3. Spatial density variations normal and parallel to the wall have similar magnitudes (cf. Fig. 3a) indicating the presence of comparable free energy barriers $\Delta u = -k_BT\ln(n/n_l)$ induced by the liquid structure along the off-plane and in-plane directions, as considered in formulating Eq. 3.

The solid-liquid interfacial energy $\gamma = -k_BT\int_0^{Ly/2} n\ln(n/n_l)dy$ is given by the energy required to remove the wetting liquid under equilibrium conditions[34,73] and can thus be determined from the 1D liquid density profile $n(y) = \iint n(x,y,z)dxdz/(L_xL_z)$ in the direction normal to a plane wall (cf. Fig. 3b). The surface energy thus determined from the liquid density profile considers both DLVO and non-DLVO interactions from liquid-liquid and liquid-solid interactions that give rise to the formation of interfacial solvation structures and solvent-induced interactions. Solid-liquid interfacial surface energies computed with this approach are reported in Fig. 3c for pairwise (wall-liquid) LJ energies e_{wl} = 0.5-1.5 k_BT that result in a range of moderate to large interfacial surface energies γ_{wl} = -0.23 to -1 k_BT/σ^2. The surface energy magnitude $|\gamma_{wl}|$ for the studied conditions increases with the pairwise LJ energy e_{wl} following a nearly quadratic relation (cf. Fig. 3c). The solid-liquid interfacial energies thus computed for a plane wall are employed to estimate the wall-liquid and particle-liquid interfacial surface energies employed in analytical expressions. The particle-liquid and wall-liquid interfacial energies with the corresponding solvation energies, and Hamaker constants for the eleven cases

$\frac{e_{pl}}{k_{BT}}$	$\frac{e_{wl}}{k_{BT}}$	$\frac{\gamma_{pl}\sigma^2}{k_BT}$	$\frac{\gamma_{wl}\sigma^2}{k_BT}$	$\frac{\lvert\bar{\gamma}\rvert\sigma^2}{k_BT}$	$\frac{U_s}{k_BT}$	$\frac{A}{k_BT}$	$\frac{A_c}{k_BT}$	$\frac{\bar{d}-d_0}{\sigma}$	$\frac{\bar{D}_\parallel}{D_0}$
1.5	1.5	-1	-1	1.00	69.1	-7.9	56.5	3.26	0.65
1.25	1.25	-0.82	-0.82	0.82	56.7	0.0	45.7	3.10	0.76
1	1	-0.6	-0.6	0.60	41.5	7.9	32.4	2.71	0.45
1	0.75	-0.6	-0.34	0.47	32.5	7.9	24.6	2.01	0.36
1	0.5	-0.6	-0.23	0.42	28.7	7.9	21.3	1.48	0.27
0.75	1	-0.34	-0.6	0.47	32.5	15.8	24.6	1.60	0.24
0.75	0.75	-0.34	-0.34	0.34	23.5	15.8	16.7	0.96	0.11
0.75	0.5	-0.34	-0.23	0.29	19.7	15.8	13.4	0.08	0.01
0.5	1	-0.23	-0.6	0.42	28.7	23.7	21.3	0.89	0.00
0.5	0.75	-0.23	-0.34	0.29	19.7	23.7	13.4	0.30	0.12
0.5	0.5	-0.23	-0.23	0.23	15.9	23.7	10.1	0.08	0.01

Table 1 Experimentally determinable model parameters for the eleven cases modeled by MD simulation. Each combination of LJ interaction energies in MD simulations produce the reported particle-liquid and wall-liquid interfacial surface energies γ_{pl} and γ_{wl}, respectively, adhesion (or dewetting) energy U_s, Hamaker constant A, and the critical contact value A_c. The average surface diffusivity $\bar{D}_\parallel$ and wall separation $\bar{d}-d_0$ are computed by averaging all MD replica simulations for each studied condition. Shaded area: predicted contact conditions for which the Hamaker constant $A > A_c$ is larger than the critical value A_c given by Eq. 6 For reference, Hamaker constants typically range from 5 to 20 k_BT for metal oxides[58–60] (e.g., SiO_2, TiO_2, ZnO) and 3 to 5 k_BT for hydrophilic polymers (e.g., PEG, PMAA) under room temperature conditions.[61–63]

studied by MD simulations are reported in Table. 1.

4 Results and discussion

This section analyzes and compares analytical predictions for the surface diffusivity from Eq. 7 using the PMF model in Eqs. 1–3 and results from the MD replica simulations described in Sec. 3 for a set of eleven conditions with the experimentally determinable parameters described in Table 1. The parameters reported in Table 1 with a range of weakly repulsive to strongly attractive Hamaker constants A/k_BT = -7.9 to 23.7 and weakly to moderately strong surfaces energies $\bar{\gamma}\sigma^2/k_BT$ = -0.23 to -1.0, correspond to a small quasi-spherical nanoparticle ($R = 6\sigma \simeq 4$ nm) of weakly to moderately wettable materials dispersed in simple molecular solvents, such as metal oxides and hydrophilic polymers in aqueous solutions. The retention of substantial in-plane mobility after physical adsorption, while the nanoparticle is kinetically trapped at finite metastable separations from the solid wall, is predicted for the cases for which $A \lesssim 65.7\bar{\gamma}\sigma^2$ according to Eq. 6 (see exposed region in Table 1).[38]

Nanoparticle surface diffusivity. To determine the separation-dependent surface diffusivity from the MD replica simulations we compute the in-plane MSD after adhesion or contact

$$MSD_\parallel(\Delta t, \bar{d}) = \frac{1}{N}\sum_{i=1}^{N}(s(t_i+\Delta t)-s(t_i))^2 \;\text{ for }\; |d_j(t_i)-\bar{d}| < \frac{\sigma}{2}, \quad (9)$$

for lag times $0 < \Delta t \leq T_s - T_a$ by using only the N parallel displacements for which the wall-particle separation is within half a molecular diameter from the average adhesion distance $\bar{d} = (1/N)\sum d(t_i > T_a)$. As reported in Fig. 4a-c, the in-plane MSD computed from MD simulations via Eq. 9 increases linearly with the lag times for finite lag times $\Delta t \gtrsim 0.2\sigma^2/D_0$. The effective surface diffusivity in MD simulations (cf. Fig. 3b) is therefore readily determined from the standard Brownian diffusion relationship

$$MSD_\parallel(\Delta t, d) = 2D_\parallel(d)\times\Delta t \quad (10)$$

by using linear regression for the finite range of lag times corresponding to $0.2\sigma^2/D_0 \leq D_0\Delta t/\sigma^2 \leq 2$, which yields very high R-square values $R^2 = 0.96$-0.98 for all the studied cases. The surface diffusivities computed via Eqs.9–10 and corresponding R-squared values did not show significant variation when increasing the upper bound of the lag time range employed for linear regression.

The average particle-wall separation $\bar{d}$ and surface diffusivity $\bar{D}_\parallel$ computed from the five replica simulations for each studied condition are reported in Table 1. The averaged results show a gradual increase of the particle-wall separation and average surface diffusivity with the magnitude of the interfacial surface energies that characterize the degree of wettability of the particle and wall surfaces. Notably, the cases for which the particle Hamaker constant A is larger than the critical contact value A_c predicted by Eq. 6 (see shaded area in Table 1) report a noticeable reduction of the average surface diffusivity, as expected when direct "dry" contact between the particle and the wall is attained.

The in-plane mean square displacement and separation-dependent surface diffusivity $D_\parallel(d)$ reported in Fig. 4 for individual replica simulations provides a more detailed picture of the complex post-adsorption behavior with stick-slip motion or immobilization randomly occurring at different separations from the wall. As showed in Fig. 4a-c the surface diffusivity $D_\parallel(d)$ for individual simulations for the same studied conditions can differ significantly from the average surface diffusivity as the Hamaker constant increases and/or the interfacial energy magnitude decreases. We compare in Fig. 4d the separation-dependent surface diffusivity $D_\parallel(d)$ predicted by the analytical model in Eq. 7 for the case of vanishingly small in-plane energy barriers $\beta = 0$ and for thermally activated stick-slip motion with energy barriers comparable to the solvation energy by using $\beta = 0.25$ & 1 in Eq. 3. The surface diffusivities determined from MD simulations (see markers in Fig. 4d) are reported for the average post-adsorption separations $\bar{d}$ for each of the five replicas of the eleven studied conditions. To readily compare the surface and bulk diffusivity, the results reported in Fig. 4d are normalized by the bulk diffusion constant D_0 computed in MD simulations for free-space Brownian motion (see Sec. 3).

All the surface diffusivities computed from individual MD replica simulations fall within the analytical predictions for in-plane Brownian diffusion solely hindered by hydrodynamic drag (i.e., $\beta = 0$ in Eq. 3) and stick-slip motion with activation barriers prescribed by a surface energy $\gamma_\tau = k_BT/\sigma^2$ (i.e., $\beta = 1$ in Eq. 3. First we must note that while the upper bound value $D_\parallel = D_0\lambda_\parallel \propto d^{-1}$ is solely prescribed by hydrodynamic friction and inversely proportional to the wall-particle separation, the lower surface diffusivity bound decreases exponentially with the separation distance. Hence, as the Hamaker constant decreases and/or the surface energy magnitude increases so that $A < A_c \simeq 65.7|\bar{\gamma}|\sigma^2$ and contact is prevented by kinetic effects, the surface diffusivities $D_\parallel \gtrsim 0.2D_0$ can become comparable to the free-space diffu-

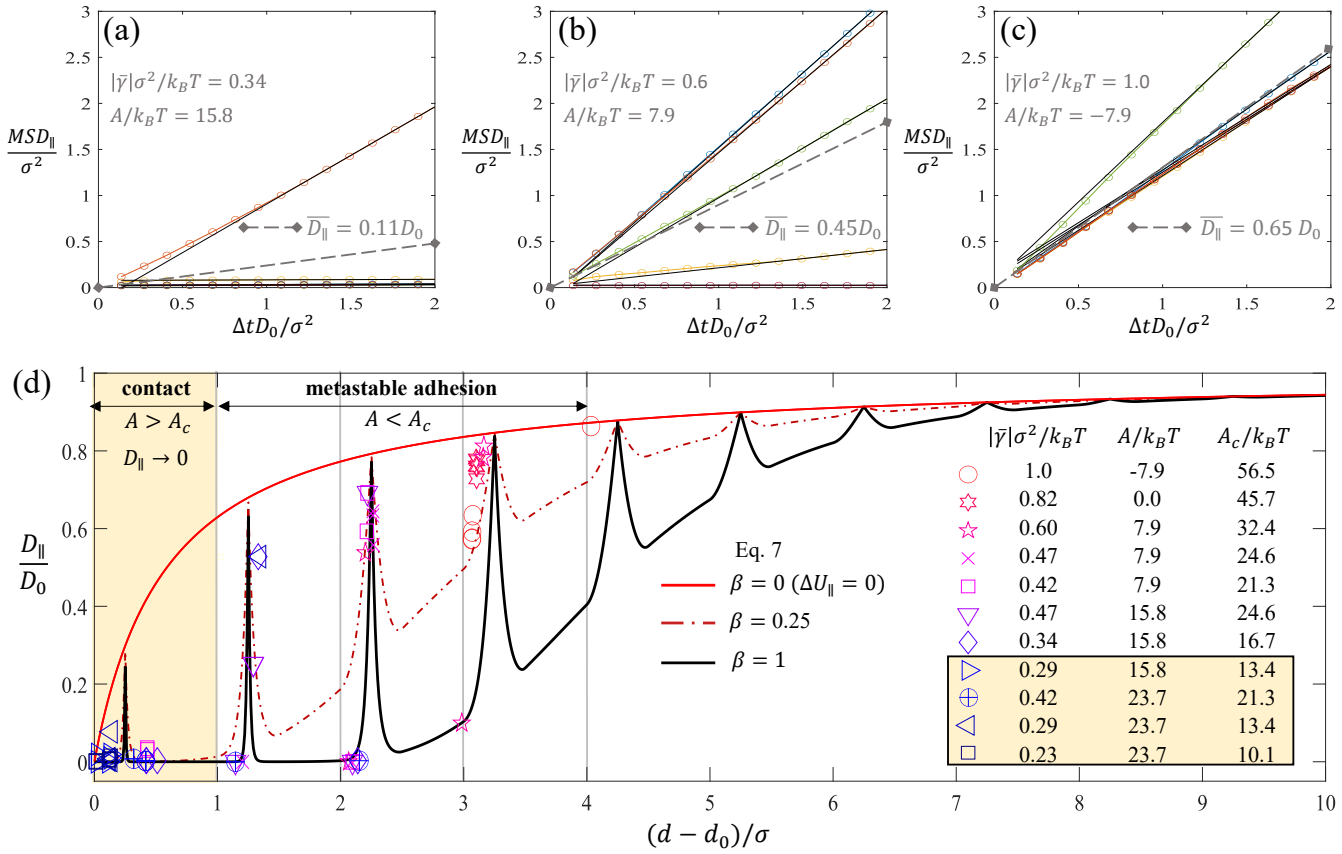

Fig. 4 In-plane mean square displacement $MSD_\parallel$ and surface diffusivity $D_\parallel$ at different adhesion separations. (a-c) $MSD_\parallel(\Delta t, d)$ vs. lag time Δt computed from individual MD replica simulations for three studied cases with surface energy magnitudes $|\bar{\gamma}| = 0.34,\ 0.6,\ \&\ 1.0\ k_BT/\sigma^2$ and Hamaker constants $A = 15.8,\ 7.9, \& -7.9\ k_BT$, respectively. Black solid lines: linear fits ($R^2 = 0.96$-0.98) to the MD data computed via Eq. 9 for individual replica simulations. Dashed grey line: MSD corresponding to the average surface diffusivity $\bar{D}$ determined using all the replica simulations for the studied case. (d) Surface diffusivity $D_\parallel(d)$ vs. separation from contact $d - d_0$ computed from individual MD replica simulations for the eleven studied cases reported in Table 1 (see legend). Analytical predictions from Eq. 7 are reported for purely hydrodynamic effects ($\Delta U_\parallel = 0$) and kinetic effects with energy barriers $\Delta U_\parallel$ comparable to the adhesion energy: $\beta = 0$ (red line), $\beta = 0.25$ (dark red dashed-dotted line), and $\beta = 1.0$ (black line). Shaded yellow regions: conditions for which $A > A_c$ and contact with vanishing surface diffusivity is expected.

sivity D_0. This analytical prediction is verified by the MD replica simulations and indicates that significant in-plane mobility can be retained after physical adsorption when either or both the particle and wall surface wettability increases. Secondly, the ability to diffuse in-plane is generally reduced when the nanoparticle is adsorbed at separations from contact $d_n - d_0 = n\sigma$ given by an integer number n of molecular liquid layers (cf. Fig. 4d). On the other hand, the surface diffusivity $D_\parallel(d) \to D_0\lambda_\parallel(d)$ increases toward the maximum value prescribed by hydrodynamic drag when the particle-wall separation is slightly larger than the metastable position and $0 < |d - d_n| < \sigma/2$, which is consistent with the analytical prediction for in-plane energy barriers in Eq. 3. This observation indicates that "defects" in the pseudo-crystalline structure of the liquid solvation layers, induced by the particle rotation, shape, and misalignment with the plane wall, can have significant effects on the effective surface diffusivity of a physically adsorbed nanoparticle.

5 Conclusions

A simple analytical model using as input a compact set of measurable or determinable parameters was formulated to predict the surface diffusivity of rigid nanoparticles physically adsorbed to a surface immersed in liquid media. While only vdW forces were considered for the studied near-contact conditions with particle-wall separations of molecular dimensions, the proposed model and analysis can be readily extended to include the electric double layer force when this is necessary. Analytical predictions from the formulated model provide the upper and lower bound for the range of random surface diffusivities reported by MD simulations of single particle adsorption over a range of physical conditions that correspond to common hydrophilic nanomaterials dispersed in aqueous solutions. While stable physical adsorption occurs for direct contact between the nanoparticle and solid surface, there are ubiquitous physicochemical conditions for which contact is prevented due to a kinetic trapping phenomenon caused by solvent-induced interactions for critically low Hamaker constants. Under such trapping conditions corresponding to "weak" attractive vdw interactions with $A \lesssim 65.7|\bar{\gamma}|\sigma^2$, nanoparticles of radius $R \gg \sigma$ can have surface diffusivities $D_\parallel \sim D_0$ comparable to the free-space diffusivity D_0, over observation times $t \gg R^2/D_0$ much larger than the characteristic diffusive time prescribed by the particle radius. Notably, the in-plane diffusivity is enhanced when

the particle remains physically adsorbed at particle-wall separations that prevent the formation of an integer number of solvation layers between the particle and wall surfaces.

An important conclusion of this work is that nanoparticles of common materials that are moderately to highly hydrophilic can produce combinations of Hamaker constant and surface energies that enable post-adsorption surface diffusion over distances larger than the particle size. Tuning the ability of a nanoparticle to remain mobile over an adsorbing surface has important implications to various technical applications that involve adhesion, transport, and removal of nanomaterials to/from wetted surfaces, or the reduction/oxidation of nanoparticles at catalytic sites on an electrode surface. The findings of this work are relevant to common nanomaterials (e.g., metal oxide nanoparticles and micro/nanoplastics) that are extensively employed in commercial applications, and are subsequently released in the environment. The proposed analytical model can be employed to guide future experimental studies, support the rational design of applications involving mass and charge transfer on wetted surfaces, and to help improve models for the environmental fate of engineered nanomaterials.

Conflicts of interest

There are no conflicts to declare.

Acknowledgements

The theoretical model development for this work was supported by the Center for Mesoscale Transport Properties, an Energy Frontier Research Center funded by the U.S. Department of Energy, Office of Science, Basic Energy Sciences, under award DE-SC0012673. T.S. acknowledges support from the National Science Foundation through award CBET-2016204. C.E.C acknowledges support from the National Science Foundation through award CBET-2417797. We thank Prof. G. Drazer for useful discussions.

Notes and references

1 J. G. Wijmans and R. W. Baker, *J. Membr. Sci.*, 1995, **107**, 1–21.
2 J. A. Brant and A. E. Childress, *J. Membr. Sci.*, 2004, **241**, 235–248.
3 S. Jiang, Y. Li and B. P. Ladewig, *Sci. Total Environ.*, 2017, **595**, 567–583.
4 K. W. Knehr, N. W. Brady, C. A. Cama, D. C. Bock, Z. Lin, C. N. Lininger, A. C. Marschilok, K. J. Takeuchi, E. S. Takeuchi and A. C. West, *J. Electrochem. Soc.*, 2015, **162**, A2817.
5 J. M. Jaksic, F. Nan, G. D. Papakonstantinou, G. A. Botton and M. M. Jaksic, *J. Phys. Chem. C*, 2015, **119**, 11267–11285.
6 C. R. Tang, L. M. Housel, C. Huang, W. Li, L. Wang, S. Yan, E. S. Takeuchi, A. C. Marschilok, C. E. Colosqui and K. J. Takeuchi, *J. Electrochem. Soc.*, 2022, **169**, 010519.
7 Q.-F. He, L. Han and D. Zhan, *Curr. Opin. Electrochem.*, 2024, 101463.
8 C. S. Mangelsdorf and L. R. White, *J. Chem. Soc., Faraday Trans.*, 1990, **86**, 2859–2870.
9 D. Stein, M. Kruithof and C. Dekker, *Phys. Rev. Lett.*, 2004, **93**, 035901.
10 C. Davidson and X. Xuan, *Electrophoresis*, 2008, **29**, 1125–1130.
11 T. J. Woehl and T. Prozorov, *J. Phys. Chem. C*, 2015, **119**, 21261–21269.
12 S. Ni, L. Isa and H. Wolf, *Soft Matter*, 2018, **14**, 2978–2995.
13 A. S. Powers, H.-G. Liao, S. N. Raja, N. D. Bronstein, A. P. Alivisatos and H. Zheng, *Nano Lett.*, 2017, **17**, 15–20.
14 A. Al Hossain, M. Yang, A. Checco, G. Doerk and C. E. Colosqui, *Appl. Mater. Today*, 2020, **19**, 100553.
15 S. Srivastava, Z. A. Wahith, O. Gang, C. E. Colosqui and S. R. Bhatia, *Adv. Mater. Interfaces*, 2020, **7**, 1901954.
16 M. Edmondson and A. Saywell, *Nano Lett.*, 2022, **22**, 8210–8215.
17 M. Wang, C. Park and T. J. Woehl, *Nanoscale*, 2022, **14**, 312–319.
18 R. Hunter, *Foundations of Colloid Science*, Oxford University Press, 2001.
19 J. N. Israelachvili, *Intermolecular and surface forces*, Academic press, 2011.
20 Z. Li and J. Zhang, *Nanoparticles and the Environment*, Springer Science & Business Media, 2012.
21 Z. Adamczyk, *Particles at interfaces: interactions, deposition, structure*, Elsevier, 2017.
22 K. Kendall, M. Kendall, F. Rehfeldt, K. Kendall, M. Kendall and F. Rehfeldt, *Adhesion of nanoparticles*, Springer, 2011.
23 D. Gentili and G. Ori, *Nanoscale*, 2022, **14**, 14385–14432.
24 P. Hänggi, P. Talkner and M. Borkovec, *Rev. Mod. Phys.*, 1990, **62**, 251.
25 D. Grolimund and M. Borkovec, *Water Resour. Res.*, 2001, **37**, 559–570.
26 I. L. Molnar, W. P. Johnson, J. I. Gerhard, C. S. Willson and D. M. O'carroll, *Water Resour. Res.*, 2015, **51**, 6804–6845.
27 N. V. Churaev, B. V. Derjaguin and V. M. Muller, *Surface forces*, Springer Science & Business Media, 2013.
28 J. Lyklema, *Fundamentals of interface and colloid science: soft colloids*, Elsevier, 2005, vol. 5.
29 R. G. Horn and J. N. Israelachvili, *J. Chem. Phys.*, 1981, **75**, 1400–1411.
30 R. M. Pashley and J. N. Israelachvili, *J. Colloid Interface Sci.*, 1984, **101**, 511–523.
31 J. Israelachvili, *Acc. Chem. Res.*, 1987, **20**, 415–421.
32 P. A. Kralchevsky and N. D. Denkov, *Chem. Phys. Lett.*, 1995, **240**, 385–392.
33 M. Ludwig and R. von Klitzing, *Curr. Opin. Colloid Interface Sci.*, 2020, **47**, 137–152.
34 S. Huang, C. E. Colosqui, Y.-N. Young and H. A. Stone, *Soft Matter*, 2022, **18**, 4786–4791.
35 G. Drazer, J. Koplik, A. Acrivos and B. Khusid, *Phys. Rev. Lett.*, 2002, **8924**, 4501.
36 G. Drazer, B. Khusid, J. Koplik and A. Acrivos, *Phys. Rev. Lett.*, 2005, **95**, 016102.

37 G. Drazer, B. Khusid, J. Koplik and A. Acrivos, *Phys. Fluids*, 2005, **17**, 17102.

38 T. Singletary, G. Drazer, A. C. Marschilok, E. S. Takeuchi, K. J. Takeuchi and C. E. Colosqui, *Nanoscale*, 2024, **16**, 5374–5382.

39 O. M. Braun and Y. S. Kivshar, *The Frenkel-Kontorova model: concepts, methods, and applications*, Springer, 2004, vol. 18.

40 Y. Dong, A. Vadakkepatt and A. Martini, *Tribol. Lett.*, 2011, **44**, 367–386.

41 Y.-z. Hu, T.-b. Ma and H. Wang, *Friction*, 2013, **1**, 24–40.

42 C. E. Colosqui, J. S. Wexler, Y. Liu and H. A. Stone, *Phys. Rev. Fluids*, 2016, **1**, 064101.

43 A. M. Rahmani, A. Wang, V. N. Manoharan and C. E. Colosqui, *Soft Matter*, 2016, **12**, 6365–6372.

44 C. Colosqui, in *Encyclopedia of Interfacial Chemistry*, ed. K. Wandelt, Elsevier, Oxford, 2018, pp. 654 – 667.

45 G. Trefalt, S. H. Behrens and M. Borkovec, *Langmuir*, 2016, **32**, 380–400.

46 R. Podgornik, *J. Chem. Phys.*, 2018, **149**, 104701.

47 R. Zwanzig, *Proc. Natl. Acad. Sci.*, 1988, **85**, 2029–2030.

48 M. J. Skaug, A. M. Lacasta, L. Ramirez-Piscina, J. M. Sancho, K. Lindenberg and D. K. Schwartz, *Soft Matter*, 2014, **10**, 753–759.

49 C. E. Colosqui, *J. Chem. Phys.*, 2019, **150**, 181102.

50 E. Pollak and S. Miret-Artés, *ChemPhysChem*, 2023, **24**, e202300272.

51 C. E. Colosqui, J. F. Morris and J. Koplik, *Phys. Rev. Lett.*, 2013, **111**, 028302.

52 H. Faxen, *Ark. Mat. Astr. Fys.*, 1923, **17**, 1–28.

53 H. Brenner, *Chem. Eng. Sci.*, 1961, **16**, 242–251.

54 A. J. Goldman, R. G. Cox and H. Brenner, *Chem. Eng. Sci.*, 1967, **22**, 637–651.

55 J. Happel and H. Brenner, *Low Reynolds number hydrodynamics: with special applications to particulate media*, Springer Science & Business Media, 2012, vol. 1.

56 R. Zwanzig and A. K. Harrison, *J. Chem. Phys.*, 1985, **83**, 5861–5862.

57 S. G. Schultz and A. Solomon, *J. Gen. Physiol.*, 1961, **44**, 1189–1199.

58 D. B. Hough and L. R. White, *Adv. Colloid Interface Sci.*, 1980, **14**, 3–41.

59 Y. Zhang, Y. Chen, P. Westerhoff, K. Hristovski and J. C. Crittenden, *Water Res.*, 2008, **42**, 2204–2212.

60 B. Faure, G. Salazar-Alvarez and L. Bergstrom, *Langmuir*, 2011, **27**, 8659–8664.

61 J. Ortega-Vinuesa, A. Martın-Rodrıguez and R. Hidalgo-Alvarez, *J. Colloid Interface Sci.*, 1996, **184**, 259–267.

62 S. Noskov, C. Scherer and M. Maskos, *J. Chromatogr. A.*, 2013, **1274**, 151–158.

63 X. Wang, N. Bolan, D. C. Tsang, B. Sarkar, L. Bradney and Y. Li, *J. Hazard. Mater.*, 2021, **402**, 123496.

64 A. P. Thompson, H. M. Aktulga, R. Berger, D. S. Bolintineanu, W. M. Brown, P. S. Crozier, P. J. in't Veld, A. Kohlmeyer, S. G. Moore, T. D. Nguyen *et al.*, *Comput. Phys. Commun.*, 2022, **271**, 108171.

65 D. J. Evans and B. L. Holian, *J. Chem. Phys.*, 1985, **83**, 4069–4074.

66 D. Dunikov, S. Malyshenko and V. Zhakhovskii, *J. Chem. Phys.*, 2001, **115**, 6623–6631.

67 S. Toxvaerd and J. C. Dyre, *J. Chem. Phys.*, 2011, **134**, 081102.

68 C. E. Colosqui, T. Teng and A. M. Rahmani, *Phys. Rev. Lett.*, 2015, **115**, 154504.

69 S. Huang, A. M. Rahmani, T. Singletary and C. E. Colosqui, *Colloids Surf. A*, 2020, **603**, 125100.

70 T. Yin, D. Shin, J. Frechette, C. E. Colosqui and G. Drazer, *Phys. Rev. Lett.*, 2018, **121**, 238002.

71 M. Schoen and C. Hoheisel, *Mol. Phys.*, 1985, **56**, 653–672.

72 R. Rowley and M. Painter, *Int. J. Thermophys.*, 1997, **18**, 1109–1121.

73 J. S. Rowlinson and B. Widom, *Molecular theory of capillarity*, Courier Corporation, 2013.

Data Availability Statement

If accepted for publication, all data employed for this manuscript, including LAMMPS input and output files will be made available at a DRYAD-Stony Brook University repository following Findable, Accessible, Interoperable and Reusable (FAIR) guidelines.